

# Quaternion-Based Generalized Super-Twisting Algorithm for Spacecraft Attitude Control<sup>\*</sup>

Bjørn Andreas Kristiansen<sup>\*</sup> Mariusz Eivind Grøtte<sup>\*</sup>  
Jan Tommy Gravdahl<sup>\*</sup>

<sup>\*</sup> Centre for Autonomous Marine Operations and Systems, Department of Engineering Cybernetics, NTNU Norwegian University of Science and Technology, NO-7491 Trondheim, Norway (e-mails: {bjorn.a.kristiansen, mariusz.eivind.grotte, jan.tommy.gravdahl}@ntnu.no).

**Abstract:** A second-order sliding mode control, the generalized super-twisting algorithm (GSTA), is used for attitude control of a spacecraft actuated by reaction wheels for pointing and a slewing maneuver. Magnetorquers are used for reaction wheel momentum dumping. Simulation results are based on a typical CubeSat. The results produced by using the GSTA are compared to sliding mode control (SMC) and a proportional–derivative (PD) controller. The simulation shows that the GSTA performs better than the SMC for the pointing and slewing maneuvers when it comes to settling time and accuracy due to reduced chattering. Compared to the PD controller, the GSTA performs similarly under the chosen conditions, with a shorter settling time for pointing, and longer settling time for slewing. The GSTA applies a torque to the reaction wheels with lower spikes and less chattering than the PD controller.

Copyright © 2020 The Authors. This is an open access article under the CC BY-NC-ND license (<http://creativecommons.org/licenses/by-nc-nd/4.0>)

*Keywords:* guidance, navigation and control of vehicles; aerospace; sliding mode control; attitude control; generalized super-twisting algorithm

## 1. INTRODUCTION

The spacecraft attitude control problem is a well-studied topic (Wen and Kreutz-Delgado (1991), (Shrivastava and Modi, 1983), (Kristiansen et al., 2009)). Various control laws for attitude control have been proposed such as the sliding mode control (SMC) (Crassidis and Markley, 1996), (McDuffie and Shtessel, 1997), which has robustness towards modeling uncertainties and disturbances. However, an issue with SMC is chattering, which is an effect due to the signum term of the control algorithm causing a zig-zag effect in the controlled channels. A method for attenuating this effect is to hide the discontinuous signum function behind an integrator (Shtessel et al., 2014). An example of this is the super-twisting algorithm (Levant, 1993), a second-order sliding mode algorithm. The super-twisting algorithm was studied for attitude control of a spacecraft actuated by magnetorquers in (Janardhanan et al., 2012). This algorithm was further developed into the generalized super-twisting algorithm (GSTA), which is proven to be robust to bounded time-varying disturbances (Castillo et al., 2018). In practice, the GSTA has successfully been applied for attitude control of other vehicles such as articulated intervention AUVs (Borlaug et al., 2019).

In this paper we present a nonlinear spacecraft model with a control law based on GSTA. Simulation results are shown for two attitude maneuvers, pointing and slewing, of a spacecraft actuated by reaction wheels using the GSTA. These extend on the case studies presented in (Grøtte et al., 2020). While (Grøtte et al., 2020) investigates time-varying attitude control strategies using an augmented proportional-derivative controller with feedforward terms and requirements for magnetorquer control law, the contributions of this paper are to compare SMC and PD with GSTA for a slewing and pointing spacecraft using state feedback.

This paper is organized as follows: In Section 2 describes the model of the dynamics used for the simulations. The model includes attitude parameterized by unit quaternions, a dynamical model for the reaction wheels, and model of perturbations. Section 3 introduces the momentum dumping control law which is used on the magnetorquers, as well as the GSTA and the SMC that we use for attitude control with the reaction wheels. We present the simulation results using parameters for a 6U CubeSat in Section 4, while conclusions are provided in Section 5.

## 2. SPACECRAFT MODEL

In this section, we present the model of an internally actuated spacecraft.

<sup>\*</sup> The work is partly sponsored by the Research Council of Norway through the Centre of Excellence funding scheme, project number 223254, AMOS, and the MASSIVE project with project number 270959.

## 2.1 Coordinate frames

*Earth-centered inertial (ECI)* The earth-centered inertial frame  $\{i\}$  has origin at the Earth's center of mass, with the  $z$ -axis pointing through the North Pole, the  $x$ -axis pointing towards vernal equinox, and the  $y$ -axis completing the right-handed system. Vectors and derivatives with respect to the ECI frame are denoted with a superscript  $i$ .

*Orbit frame* The Vehicle Velocity, Local Horizontal (VVLH) frame, or the orbit frame  $\{o\}$ , has superscript  $o$  for vectors represented in the frame. The orbit frame is centered in the center of mass of the spacecraft. The  $z$ -,  $x$ -, and  $y$ -axis point in the direction of the Earth's center of mass, the orbit velocity vector, and in a direction that completes the right-handed coordinate system, respectively. The unit vectors of the frame are given by

$$\hat{\mathbf{z}}^o = -\frac{\mathbf{r}^i}{\|\mathbf{r}^i\|_2}, \quad \hat{\mathbf{x}}^o = \frac{\mathbf{v}^i}{\|\mathbf{v}^i\|_2}, \quad \hat{\mathbf{y}}^o = \frac{\hat{\mathbf{z}}^o \times \hat{\mathbf{x}}^o}{\|\hat{\mathbf{z}}^o \times \hat{\mathbf{x}}^o\|_2}, \quad (1)$$

where  $\mathbf{r}^i$  is the distance between the spacecraft and the center of the Earth, and  $\mathbf{v}^i$  is the inertial velocity of the spacecraft.

*Body frame* The axes of the body frame  $\{b\}$  follow the spacecraft structure, and its origin is centered in the spacecraft's center of mass. Vectors represented in this frame have superscript  $b$ .

*Wheel frame* The wheel frame  $\{w\}$  is a frame used to specify vectors directly related to the reaction wheels. The two vectors that are represented in this frame are the wheel angular velocity,  $\boldsymbol{\omega}_{bw}^w$ , and the torque applied to each wheel,  $\boldsymbol{\tau}_u^w$ . The dimension of these vectors equals the number of reaction wheels, where each channel of the vectors specifies the angular velocity or torque applied about each wheel's axis of rotation. The mapping of the wheel frames to the body frame is represented by the matrix  $\mathbf{A} \in \mathbb{R}^{3 \times n}$ , as

$$\boldsymbol{\tau}_u^b = \mathbf{A} \boldsymbol{\tau}_u^w \Rightarrow \boldsymbol{\tau}_u^w = \mathbf{A}^+ \boldsymbol{\tau}_u^b, \quad (2)$$

where  $\mathbf{A}^+$  is the pseudo-inverse of  $\mathbf{A}$ . Note that  $\mathbf{A}$  is a constant mapping between the wheel frame and the body frame due to a fixed reaction wheel configuration.

## 2.2 Attitude representation

Unit quaternions, represented as  $\mathbf{q} = [\eta \ \boldsymbol{\epsilon}]^\top = [\eta \ \epsilon_1 \ \epsilon_2 \ \epsilon_3]^\top$ , are used to describe the attitude of the spacecraft, where  $\eta$  is the scalar part of the quaternion,  $\boldsymbol{\epsilon}$  is the vector part of the quaternion and satisfies the condition  $\eta^2 + \boldsymbol{\epsilon}^\top \boldsymbol{\epsilon} = 1$ .  $\mathbf{q}_{ob}$  is denoted as the attitude of the body frame relative to the orbit frame. Similarly, the rotation matrix between the two frames is given as (Egeland and Gravdahl, 2002)

$$\mathbf{R}_b^o = \mathbf{I}_{3 \times 3} + 2\eta_{ob} \mathbf{S}(\boldsymbol{\epsilon}_{ob}) + 2\mathbf{S}^2(\boldsymbol{\epsilon}_{ob}), \quad (3)$$

where  $\mathbf{I}_{3 \times 3}$  is the three-dimensional identity matrix, and  $\mathbf{S}(\cdot)$  is a skew-symmetric matrix. The time derivative of a rotation matrix  $\mathbf{R}_o^b$  is  $\dot{\mathbf{R}}_o^b = -\mathbf{S}(\boldsymbol{\omega}_{ob}^b) \mathbf{R}_o^b$ , where  $\boldsymbol{\omega}_{ob}^b$  denotes the angular velocity of  $\{b\}$  relative to  $\{o\}$ .

The kinematic differential equation for  $\mathbf{q}_{ob}$  is given by

$$\dot{\mathbf{q}}_{ob} = \begin{bmatrix} \dot{\eta}_{ob} \\ \dot{\boldsymbol{\epsilon}}_{ob} \end{bmatrix} = \frac{1}{2} \begin{bmatrix} -\boldsymbol{\epsilon}_{ob}^\top \\ \eta_{ob} \mathbf{I}_{3 \times 3} + \mathbf{S}(\boldsymbol{\epsilon}_{ob}) \end{bmatrix} \boldsymbol{\omega}_{ob}^b = \frac{1}{2} \mathbf{T}(\mathbf{q}_e) \boldsymbol{\omega}_{ob}^b. \quad (4)$$

where  $\mathbf{T}(\cdot)$  is the angular velocity transformation matrix.

## 2.3 Angular velocity

The angular velocity of the spacecraft's body frame relative to the orbit frame is given as

$$\boldsymbol{\omega}_{ob}^b = \boldsymbol{\omega}_{ib}^b - \boldsymbol{\omega}_{io}^b = \boldsymbol{\omega}_{ib}^b - \mathbf{R}_o^b \boldsymbol{\omega}_{io}^o, \quad (5)$$

where  $\boldsymbol{\omega}_{io}^o$  is the angular velocity of the  $\{o\}$  relative to the  $\{i\}$ , and  $\boldsymbol{\omega}_{ib}^b$  is the angular velocity of the  $\{b\}$  relative to the  $\{i\}$ .

The angular velocity of the  $\{o\}$  frame relative to  $\{i\}$ , denoted  $\boldsymbol{\omega}_{io}^o$ , is defined in Oland and Schlanbusch (2009) as

$$\boldsymbol{\omega}_{io}^o = \mathbf{R}_i^o \frac{\mathbf{S}(\mathbf{r}^i) \mathbf{v}^i}{(\mathbf{r}^i)^\top \mathbf{r}^i}. \quad (6)$$

## 2.4 Attitude dynamics

The total system inertia of the spacecraft rigid body is given by  $\mathbf{J} \in \mathbb{R}^{3 \times 3}$ , such that

$$\mathbf{J} = \mathbf{J}_s + \mathbf{A} \mathbf{J}_w \mathbf{A}^\top, \quad (7)$$

where the inertia of the rigid body excluding the inertia about the spinning axis of the reaction wheels is  $\mathbf{J}_s \in \mathbb{R}^{3 \times 3}$ , and the inertia matrix of the reaction wheels about the spinning axes is  $\mathbf{J}_w \in \mathbb{R}^{n \times n}$ .

The total angular momentum of the spacecraft is given as (Krogstad and Gravdahl, 2006)

$$\mathbf{H}_s^b = \mathbf{J} \boldsymbol{\omega}_{ib}^b + \mathbf{A} \mathbf{J}_w \boldsymbol{\omega}_{bw}^w. \quad (8)$$

Using Euler's second axiom, the rigid body dynamics is

$$\mathbf{J} \frac{d}{dt} \boldsymbol{\omega}_{ib}^b + \mathbf{A} \mathbf{J}_w \frac{d}{dt} \boldsymbol{\omega}_{bw}^w + \mathbf{S}(\boldsymbol{\omega}_{ib}^b) \mathbf{H}_s^b = \boldsymbol{\tau}_{mtq}^b + \boldsymbol{\tau}_{ext}^b, \quad (9)$$

where  $\boldsymbol{\tau}_{mtq}^b$  is the torque produced by the magnetorquers and  $\boldsymbol{\tau}_{ext}^b$  is the external perturbation torque acting on the spacecraft.

## 2.5 Perturbations

The total perturbing torque is given by

$$\boldsymbol{\tau}_{ext}^b = \boldsymbol{\tau}_{drag}^b + \boldsymbol{\tau}_{srp}^b + \boldsymbol{\tau}_{grav}^b + \boldsymbol{\tau}_{mag}^b, \quad (10)$$

where  $\boldsymbol{\tau}_{drag}^b$  is the torque due to aerodynamic drag,  $\boldsymbol{\tau}_{srp}^b$  is the torque due to solar radiation pressure,  $\boldsymbol{\tau}_{grav}^b$  is the torque due to the gravity gradient, and  $\boldsymbol{\tau}_{mag}^b$  is the torque due to the interaction between internal spacecraft electronics and the Earth's magnetic field.

*Aerodynamic drag* Aerodynamic drag is given by

$$\mathbf{F}_{drag}^b = -\frac{1}{2} \rho A_{drag} \|\mathbf{v}^b\|^2 C_D \frac{\mathbf{v}^b}{\|\mathbf{v}^b\|}, \quad (11)$$

where  $\rho$  is the density of the atmosphere at a given altitude,  $C_D$  is the drag coefficient, and  $A_{drag}$  is the surface area affected by the contact force. For simplicity, the surface area of the largest face of the spacecraft is chosen.

We use a simplified version of the torque produced by the aerodynamic drag

$$\boldsymbol{\tau}_{drag}^b = (\mathbf{x}_{CP}^b - \mathbf{x}_{CG}^b) \times \mathbf{F}_{drag}^b, \quad (12)$$

where  $\mathbf{x}_{CP}^b$  is the center of pressure and  $\mathbf{x}_{CG}^b$  is the center of gravity. The vectors are chosen such that the distance between the centers are as large as possible but limited by the spacecraft structure size.

*Gravity gradient* The gravity gradient torque is due to the spacecraft not being a point mass when modeling the rigid body dynamics. It is given in Hughes (2004) as

$$\boldsymbol{\tau}_{\text{grav}}^b = 3 \frac{\mu}{\|\mathbf{r}^i\|^3} \mathbf{S}(\mathbf{c}_3) \mathbf{J} \mathbf{c}_3, \quad (13)$$

where  $\mathbf{c}_3$  is the third column vector of  $\mathbf{R}_o^b$ .

*Solar radiation pressure* We use a simplified model for the solar radiation pressure, where the sun's position is constant in the inertial frame, and the surface area that is affected by the sunlight is assumed to be the largest face of the spacecraft. Another simplification made is that the solar radiation pressure is constantly applied. Together these eliminate the need to model the sun's actual position. These simplifications do not represent an accurate model of the sun's effect on the system, but they are sufficient in order to simulate the worst-case effect of solar radiation with respect to attitude control in a relatively brief time. The force is given by (Gravdahl et al., 2003)

$$\mathbf{F}_{\text{srp}}^b = \mathbf{R}_i^b \frac{F_{\text{srp}}}{c} A_{\text{srp}} (1+l) \cos(\alpha) [0 \ 1 \ 0]^T, \quad (14)$$

where  $F_{\text{srp}}$  is the solar constant,  $c$  is the speed of light in vacuum,  $A_{\text{srp}}$  represent the maximum exposed surface area,  $l$  is the reflectance, and  $\alpha$  is the incidence angle of the incoming light. The values for  $A_{\text{srp}}$ ,  $\alpha$ , and the direction vector are chosen to maximize the absolute value of the force.

The corresponding torque is given as

$$\boldsymbol{\tau}_{\text{srp}}^b = (\mathbf{x}_{CP}^b - \mathbf{x}_{CG}^b) \times \mathbf{F}_{\text{srp}}^b. \quad (15)$$

The center of pressure and the center of gravity are chosen in the same manner as they were for the aerodynamic drag torque.

*Magnetic torque* The magnetic torque is created due to the spacecraft's electronics setting up a dipole that interacts with the Earth's magnetic field. The magnetic torque is given by

$$\boldsymbol{\tau}_{\text{mag}}^b = (D \sqrt{\frac{1}{3}} \cdot [1, 1, 1]^T) \times \mathbf{B}^b, \quad (16)$$

where  $D$  is a constant representing the size of the residual magnetic dipole, and  $\mathbf{B}^b$  is the body frame vector of the Earth's magnetic field. The latter is represented by the IGRF (International Geomagnetic Reference Field) model in the simulations.

## 2.6 Reaction wheel dynamics

The angular momentum of the reaction wheels is given as (Krogstad and Gravdahl, 2006)

$$\mathbf{H}_w^b = \mathbf{A} \mathbf{J}_w \mathbf{A}^T (\boldsymbol{\omega}_{ib}^b + \mathbf{A} \boldsymbol{\omega}_{bw}^w) = \mathbf{A} \mathbf{J}_w \boldsymbol{\omega}_{iw}^w = \mathbf{A} \mathbf{J}_w \mathbf{A}^T \boldsymbol{\omega}_{iw}^b. \quad (17)$$

We find the reaction wheel dynamics by applying Euler's second axiom,

$$\begin{aligned} \frac{d}{dt} \mathbf{H}_w^b &= \frac{d}{dt} (\mathbf{A} \mathbf{J}_w \mathbf{A}^T \boldsymbol{\omega}_{iw}^b) + \mathbf{S}(\boldsymbol{\omega}_{iw}^b) \mathbf{H}_w^b \\ &= \mathbf{A} \mathbf{J}_w \mathbf{A}^T \frac{d}{dt} \boldsymbol{\omega}_{iw}^b + \mathbf{S}(\mathbf{A} \boldsymbol{\omega}_{iw}^w) (\mathbf{A} \mathbf{J}_w \boldsymbol{\omega}_{iw}^w) = \mathbf{A} \mathbf{J}_w \mathbf{A}^T \frac{d}{dt} \boldsymbol{\omega}_{iw}^b \\ &= \mathbf{A} \mathbf{J}_w \mathbf{A}^T \left( \frac{d}{dt} \boldsymbol{\omega}_{ib}^b + \mathbf{A} \frac{d}{dt} \boldsymbol{\omega}_{bw}^w \right) = \boldsymbol{\tau}_u^b = \mathbf{A} \boldsymbol{\tau}_u^w, \end{aligned} \quad (18)$$

where we have used that

$$\mathbf{S}(\mathbf{A} \boldsymbol{\omega}_{iw}^w) (\mathbf{A} \mathbf{J}_w \boldsymbol{\omega}_{iw}^w) = 0 \quad (19)$$

when the inertia of the reaction wheels are equal.

## 2.7 Attitude error dynamics

The attitude error variables are defined as

$$\mathbf{q}_e = \mathbf{q}_d^{-1} \otimes \mathbf{q}_{ob} = \begin{bmatrix} \eta_d & \boldsymbol{\epsilon}_d^T \\ -\boldsymbol{\epsilon}_d & \eta_d \mathbf{I}_{3 \times 3} - \mathbf{S}(\boldsymbol{\epsilon}_d) \end{bmatrix} \mathbf{q}_{ob} \quad (20)$$

where  $\eta_d$  and  $\boldsymbol{\epsilon}_d$  are the scalar and vector part of the desired quaternion  $\mathbf{q}_d$ , respectively, and

$$\boldsymbol{\omega}_e^b = \boldsymbol{\omega}_{ob}^b - \boldsymbol{\omega}_d^b = \boldsymbol{\omega}_{ib}^b - \mathbf{R}_o^b \boldsymbol{\omega}_{io}^o - \boldsymbol{\omega}_d^b, \quad (21)$$

where  $\boldsymbol{\omega}_d^b$  represents the desired angular velocity. We find the angular velocity error dynamics by differentiating Equation (21) with respect to time. Specifically,

$$\begin{aligned} \frac{d}{dt} (\mathbf{R}_o^b \boldsymbol{\omega}_{io}^o) &= \frac{d}{dt} (\mathbf{R}_o^b) \boldsymbol{\omega}_{io}^o + \mathbf{R}_o^b \frac{d}{dt} (\boldsymbol{\omega}_{io}^o) \\ &= -\mathbf{S}(\boldsymbol{\omega}_{ob}^b) \mathbf{R}_o^b \boldsymbol{\omega}_{io}^o - \mathbf{R}_o^b \mathbf{S}(\boldsymbol{\omega}_{ob}^o) \boldsymbol{\omega}_{io}^o, \end{aligned} \quad (22)$$

where we have used that the orbit is constant over time. Equation (18) can be used to rewrite (9) by taking advantage of (7),

$$\begin{aligned} \mathbf{J}_s \frac{d}{dt} \boldsymbol{\omega}_{ib}^b &= -(\mathbf{A} \mathbf{J}_s \mathbf{A}^T \frac{d}{dt} \boldsymbol{\omega}_{ib}^b + \mathbf{A} \mathbf{J}_w \frac{d}{dt} \boldsymbol{\omega}_{bw}^w) - \mathbf{S}(\boldsymbol{\omega}_{ib}^b) \mathbf{H}_s^b \\ &\quad + \boldsymbol{\tau}_{\text{mtq}}^b + \boldsymbol{\tau}_{\text{ext}}^b = -\mathbf{A} \boldsymbol{\tau}_u^w - \mathbf{S}(\boldsymbol{\omega}_{ib}^b) \mathbf{H}_s^b + \boldsymbol{\tau}_{\text{mtq}}^b + \boldsymbol{\tau}_{\text{ext}}^b \end{aligned} \quad (23)$$

From (20), (21), (22), and (23), the error dynamics become

$$\dot{\mathbf{q}}_e = \frac{1}{2} \mathbf{T}(\mathbf{q}_e) \boldsymbol{\omega}_e^b, \quad (24)$$

$$\begin{aligned} \mathbf{J}_s \frac{d}{dt} \boldsymbol{\omega}_e^b &= -\mathbf{S}(\boldsymbol{\omega}_{ib}^b) \mathbf{H}_s^b - \mathbf{A} \boldsymbol{\tau}_u^w + \boldsymbol{\tau}_{\text{mtq}}^b + \boldsymbol{\tau}_{\text{ext}}^b \\ &\quad + \mathbf{J}_s \mathbf{S}(\boldsymbol{\omega}_{ob}^b) \mathbf{R}_o^b \boldsymbol{\omega}_{io}^o + \mathbf{J}_s \mathbf{R}_o^b \mathbf{S}(\mathbf{R}_o^b \boldsymbol{\omega}_{ob}^o) \boldsymbol{\omega}_{io}^o - \mathbf{J}_s \frac{d}{dt} \boldsymbol{\omega}_d^b. \end{aligned} \quad (25)$$

## 3. CONTROL DESIGN

In this section, we present the control algorithms we use on the spacecraft's actuators. The main actuator for attitude control will in this paper be the reaction wheels. A momentum dumping controller is used to counteract momentum building up in the reaction wheels. We use the magnetorquers to provide the external torque required for the momentum dumping.

### 3.1 Momentum dumping controller

The momentum dumping control law is given as (Markley and Crassidis, 2014)

$$\boldsymbol{\tau}_{\text{mtq}} = \mathbf{m}^b \times \mathbf{B}^b = \left( \frac{k_m}{\|\mathbf{B}^b\|_2} (\mathbf{h}_e^b \times \mathbf{B}^b) \right) \times \mathbf{B}^b, \quad (26)$$

where  $\mathbf{m}^b$  is the magnetic moment,  $k_m$  is a positive constant, and  $\mathbf{h}_e^b$  is the error in angular momentum for the reaction wheels, given as

$$\mathbf{h}_e^b = \mathbf{A} \mathbf{J}_w (\boldsymbol{\omega}_{bw}^w - \boldsymbol{\omega}_{bw,\text{ref}}^w), \quad (27)$$

where  $\boldsymbol{\omega}_{bw,\text{ref}}^w$  is the reference speed of the reaction wheels.

### 3.2 Generalized super-twisting algorithm (GSTA)

The generalized super-twisting algorithm is proposed here to control the attitude with the reaction wheels. The GSTA is a second order sliding mode control algorithm which is robust to bounded time-varying disturbances, such as the environmental torques  $\tau_{\text{ext}}^b$ . The GSTA is given as

$$\begin{aligned}\tau_u^b &= (-1) \cdot (-\mathbf{k}_1 \phi(\boldsymbol{\sigma})_1 + \mathbf{z}), \\ \dot{\mathbf{z}} &= -\mathbf{k}_2 \phi(\boldsymbol{\sigma})_2, \\ \phi_1(\boldsymbol{\sigma}) &= [\boldsymbol{\sigma}]^{\frac{1}{2}} + \boldsymbol{\beta} \boldsymbol{\sigma}, \\ \phi_2(\boldsymbol{\sigma}) &= \frac{1}{2} [\boldsymbol{\sigma}]^0 + \frac{3}{2} \boldsymbol{\beta} [\boldsymbol{\sigma}]^{\frac{1}{2}} + \boldsymbol{\beta}^2 \boldsymbol{\sigma},\end{aligned}\quad (28)$$

where  $\mathbf{k}_1, \mathbf{k}_2$ , and  $\boldsymbol{\beta}$  are positive and constant positive controller gain vectors that are applied element-wise,  $\boldsymbol{\sigma}$  is the sliding surface, and the function  $[\cdot]^x$  is defined as  $[a]^b = |a|^b \text{sign}(a)$ , which is applied element-wise when the argument  $a$  is a vector.

*Surface for pointing* For pointing, we propose the sliding surface

$$\boldsymbol{\sigma}_p = \boldsymbol{\epsilon}_e^b + \mathbf{K} \boldsymbol{\epsilon}_e^b, \mathbf{K} > 0, \quad (29)$$

where  $\boldsymbol{\epsilon}_e^b$  is the vector part of the error quaternion. On the sliding surface,  $\boldsymbol{\sigma}_p = \mathbf{0}$ , such that  $\dot{\boldsymbol{\epsilon}}_e^b = -\mathbf{K} \boldsymbol{\epsilon}_e^b$ , and thus the origin  $\boldsymbol{\epsilon}_e^b = \mathbf{0}$  is asymptotically stable. As the unit quaternion is defined to have a length equal to one, the surface will have two asymptotically stable equilibrium points in  $\boldsymbol{\epsilon}_e = \mathbf{0}, \eta_e = \pm 1$ .

*Surface for slewing* We use a sliding surface based on Fjellstad and Fossen (1994) for slewing, given as

$$\boldsymbol{\sigma}_s = \boldsymbol{\omega}_e^b - 2c_1 \frac{\partial W}{\partial \eta_e} \boldsymbol{\epsilon}_e, \quad (30)$$

where  $c_1$  is a positive constant, and  $W$  is a Lyapunov function candidate (LFC) chosen to be  $W = 1 - |\eta_e|$ . From this choice, the surface becomes

$$\boldsymbol{\sigma}_s = \boldsymbol{\omega}_e^b + 2c_1 \text{sgn}(\eta_e) \boldsymbol{\epsilon}_e. \quad (31)$$

Note that the signum function is defined to be positive when evaluated at zero. Based on the proof in Fjellstad and Fossen (1994), a sketch of the proof showing asymptotic stability for the chosen sliding surface is as follows:

Differentiating the general LFC  $W(\eta_e)$  yields

$$\frac{d}{dt} W(\eta_e) = \frac{\partial W}{\partial \eta_e} \frac{\partial \eta_e}{\partial t} = \frac{\partial W}{\partial \eta_e} \left(-\frac{1}{2} \boldsymbol{\epsilon}_e^T \boldsymbol{\omega}_e^b\right) = -c_1 \left(\frac{\partial W}{\partial \eta_e}\right)^2 \boldsymbol{\epsilon}_e^T \boldsymbol{\epsilon}_e, \quad (32)$$

where Equation (30) set to zero has been used to define  $\boldsymbol{\omega}_e^b$ . The time derivative of the LFC is negative definite for all  $\boldsymbol{\epsilon}_e \neq \mathbf{0}$  as long as  $W(\eta_e)$  is chosen such that  $\frac{\partial W}{\partial \eta_e}$  is always non-zero. The LFC

$$W(\eta_e) = 1 - |\eta_e|, \quad (33)$$

satisfies this constraint since  $\frac{\partial W}{\partial \eta_e} = -\text{sgn}(\eta_e)$ . The LFC is positive definite and the time derivative

$$\frac{d}{dt} W(\eta_e) = -c_1 \left(\frac{\partial W}{\partial \eta_e}\right)^2 \boldsymbol{\epsilon}_e^T \boldsymbol{\epsilon}_e = -c_1 \boldsymbol{\epsilon}_e^T \boldsymbol{\epsilon}_e, \quad (34)$$

is negative definite, and from this we can use Lyapunov's second method to conclude that the two equilibrium points of the quaternion representation ( $\eta_e = \pm 1, \boldsymbol{\epsilon}_e = \mathbf{0}$ ) are asymptotically stable. This conclusion only holds when the signum function is defined as non-zero.

### 3.3 Sliding mode control (SMC)

Sliding mode control (SMC) is given as

$$\tau_u^b = \mathbf{k} \text{sgn}(\boldsymbol{\sigma}), \quad (35)$$

where  $\boldsymbol{\sigma}$  is the sliding surface, defined as for the GSTA, and  $\mathbf{k}$  is a constant (positive) controller gain vector that is applied element-wise.

### 3.4 Proportional-derivative controller (PD)

The PD controller is given as (Wen and Kreutz-Delgado, 1991)

$$\tau_u^b = \mathbf{K}_d \boldsymbol{\omega}_e^b + \mathbf{K}_p \boldsymbol{\epsilon}_e \quad (36)$$

where  $\mathbf{K}_d$  and  $\mathbf{K}_p$  are constant (positive definite) controller gain matrices, with numerical values to be chosen when tuning the controller.

## 4. SIMULATION

In this section, we present the numerical simulations based on spacecraft attitude control scenarios with two maneuvers: pointing and slewing. We compare the response of the controlled variables with GSTA, SMC, and PD controller.

### 4.1 Setup

A 6U CubeSat model is chosen as the spacecraft rigid body in this simulation. It has magnetorquers on all three body axes and four reaction wheels. Three reaction wheels are separately fixed on each of the three body axes, and a fourth is tilted such that the resulting torque has equal components in each axis in body frame. The torque distribution matrix is given as

$$\mathbf{A} = \frac{1}{3} \begin{bmatrix} 3 & 0 & 0 & \sqrt{3} \\ 0 & 3 & 0 & \sqrt{3} \\ 0 & 0 & 3 & \sqrt{3} \end{bmatrix}. \quad (37)$$

The total inertia matrix and the reaction wheel inertia matrix are given as

$$\mathbf{J} = \begin{bmatrix} 0.0775 & 0.0002 & -0.0002 \\ 0.0002 & 0.1067 & 0.0005 \\ -0.0002 & 0.0005 & 0.0389 \end{bmatrix} \text{ kg m}^2, \quad \mathbf{J}_w = I_w \mathbf{I}_{4 \times 4}, \quad (38)$$

where  $I_w = 2.1 \cdot 10^{-4} \text{ kg m}^2$  is the inertia of a single reaction wheel, which are all set to be identical.  $\mathbf{J}_s$  is found by combining (37) and (38) with (7).

Parameters used in simulations are shown in Tables 1-5.

Table 1. Orbital elements of initial orbit

Orbital element	Value
Semimajor axis	6852.2 km
Eccentricity	0.002
Inclination	97°
Right ascension of the ascending node	280°
Argument of periapsis	0°
True anomaly	90°

The orbit represented by the parameters in Table 1 is a commonly chosen Low-Earth-Orbit (LEO) for remote sensing. In Table 4, the reaction wheel jittering is modeled based on friction and speed resolution in the reaction

Table 2. Physical parameters

Physical parameter	Value
CubeSat mass	7 kg
CubeSat surface area ( $A_{srp}, A_{drag}$ )	0.06 m <sup>2</sup>
Earth Radius	$6.371 \cdot 10^6$ m
Standard grav. parameter, Earth ( $\mu$ )	$3.986 \cdot 10^{14}$ m <sup>3</sup> /s <sup>2</sup>
Atmospheric density ( $\rho$ )	$1.7741 \cdot 10^{-12}$ kg/m <sup>3</sup>
Drag coefficient ( $C_D$ )	2.1
Solar constant ( $F_{srp}$ )	1367 W/m <sup>2</sup>
Speed of light in vacuum ( $c$ )	$3 \cdot 10^8$ m/s
Reflectance, satellite ( $l$ )	0.2
Angle of sunlight on the satellite ( $\alpha$ )	0°
Residual magnetic dipole ( $D$ )	$1 \cdot 10^{-2}$

Table 3. Saturation bounds

Saturation bounds	Value
Reaction wheel angular velocity	$\pm 5000$ RPM
Reaction wheel angular velocity, rate	$\pm 4.5 \cdot 10^3$ rad/s <sup>2</sup>
Reaction wheel input torque	$\pm 3 \cdot 10^{-3}$ Nm
Magnetorquer magnetic moment	$\pm 5 \cdot 10^{-1}$ Am <sup>2</sup>

Table 4. Noise

Noise	Value
Reaction wheel jittering	3 RPM
$\omega_{ib}^b$ noise	$6.9813 \cdot 10^{-8}$ rad/s

Table 5. Controller gains

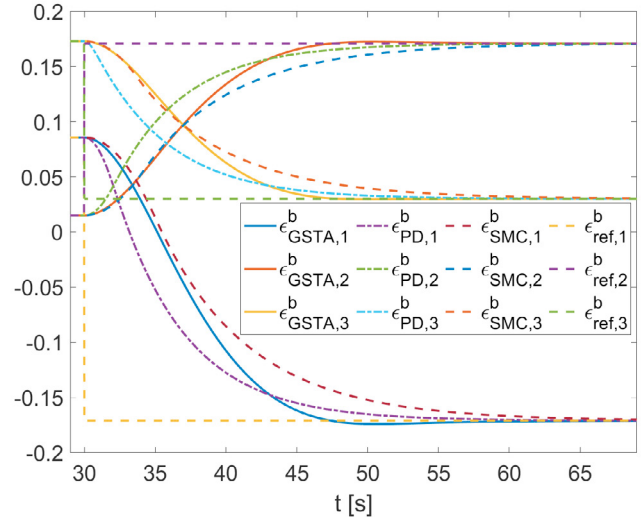
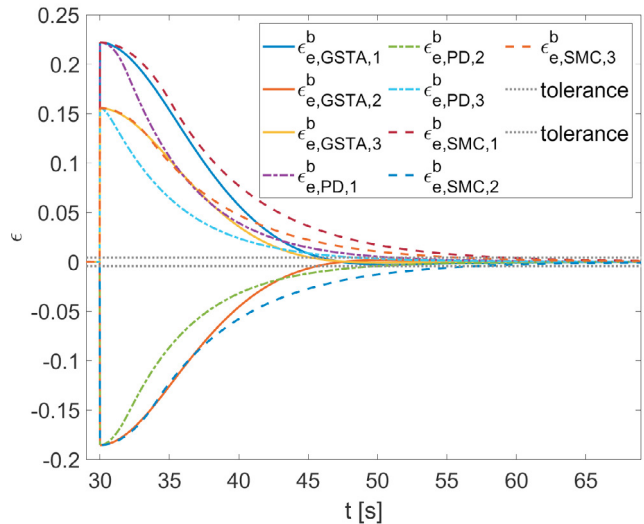
Controller gain	Value
$k_m$ (mtq)	$1.5 \cdot 10^{-2}$
$\mathbf{K}$ (surface)	$0.15 \cdot \mathbf{I}_{3 \times 3}$
$\mathbf{k}_1$ (GSTA)	$\frac{2.5}{1000} \mathbf{J}_s \cdot \mathbf{1}_{3 \times 1}$
$\mathbf{k}_2$ (GSTA)	$(2 \cdot 10^{-8}) \mathbf{1}_{3 \times 1}$
$\beta$ (GSTA)	$15 \cdot \mathbf{1}_{3 \times 1}$
$\mathbf{K}_p$ (PD, point)	$\mathbf{J}_s$
$\mathbf{K}_p$ (PD, slew)	$0.01 \mathbf{J}_s$
$\mathbf{K}_d$ (PD)	$2.7 \mathbf{J}_s$
$\mathbf{k}$ (SMC, point)	$0.01 \mathbf{J}_s \cdot \mathbf{1}_{3 \times 1}$
$\mathbf{k}$ (SMC, slew)	$\frac{2}{1250} \mathbf{J}_s \cdot \mathbf{1}_{3 \times 1}$
$c_1$ (GSTA, slew)	2
$c_1$ (SMC, slew)	$2 \cdot 10^{-3}$

wheels, while the  $\omega_{ib}^b$  noise is due to unwanted thermal and structural effects. Perfect attitude knowledge is assumed.

For the momentum dumping controller, the reference reaction wheel speed  $\omega_{bw,ref}^w$  is set to  $2000 \cdot [1 \ 1 \ 1 \ -\sqrt{3}]^T$  RPM. At this point, the angular momentum created by the reaction wheels will be net zero about the axes in  $\{b\}$ .

#### 4.2 Performance measures

The performance is measured using root-mean-square error (RMSE) of stationary signals. We define the signal to be stationary when it has settled, meaning when it stays inside a given error band around the target value. The error band is defined to be  $\pm 0.5^\circ$  for pointing, and  $\pm 4 \cdot 10^{-4}$  rad/s for slewing. The settling time is the time it takes from applying the desired reference value to the error band being reached and stays within the error band. The steady-state error (SSE) for each channel is measured at the end of each simulation.


 Fig. 1. Pointing: Plot of the vector part of  $\mathbf{q}$  and  $\mathbf{q}_d$ .

 Fig. 2. Pointing: Plot of the vector part of  $\mathbf{q}_e$ .

#### 4.3 Pointing

Pointing is a fixed-vector orientation towards a desired attitude. Both the GSTA and the SMC use the surface defined in Equation (29).

Table 6. Pointing performance

	Settling time	RMSE	SSE
GSTA	[15.9, 15.7, 15.2]s	[4.80, 3.14, 2.43]*	[0.5, 0.0, 0.0]*
PD	[21, 20, 18.4]s	[4.24, 4.22, 4.24]*	[0.5, 0.0, 0.1]*
SMC	[29.1, 27.2, 25.8]s	[4.93, 4.91, 4.88]*	[0.6, 0.0, 0.1]*

The star (\*) in Table 6 denotes  $10^{-2}$  angular degrees ( $^\circ$ ). Figures 1, 2, and 3 are centered around the transient period of the control. Figures 4, 5, and 6 are plots over a longer time to show the effects of attitude control and momentum dumping controller on the reaction wheel speed. For pointing, the objective is illustrated in Figure 1, where a slight overshoot can be seen in the GSTA response. In the the error variables shown in Figure 2, it can be seen that this overshoot does not result in the signal escaping the error band and indicating that the performance of

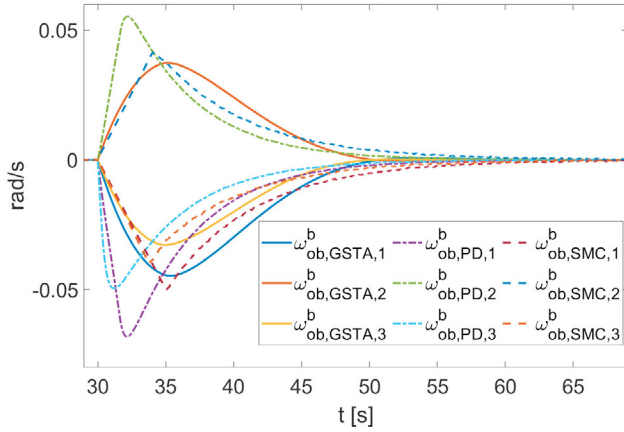


Fig. 3. Pointing: Plot of  $\omega_{ob}^b$ .

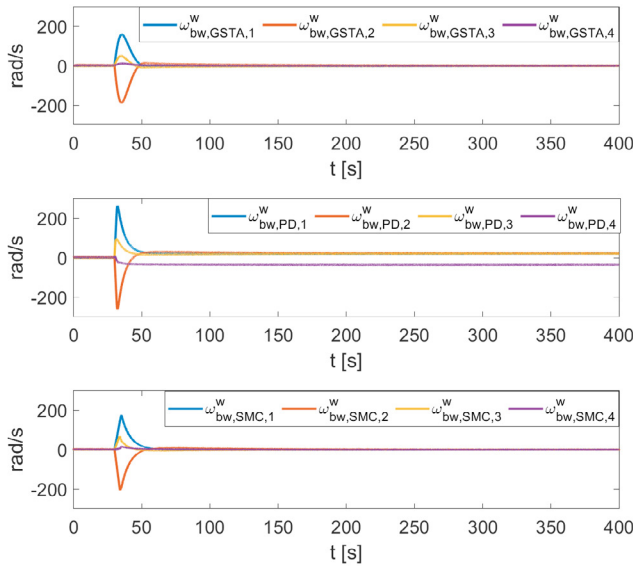


Fig. 4. Pointing: Plot of  $\omega_{bw}^w - \omega_{bw,ref}^w$ .

GSTA is better than that of PD controller and SMC. It is also performing better with respect to settling time across all channels: between four and five seconds for the PD controller, and over 10 seconds for the SMC.

As seen in Figure 2, the PD controller converges fastest initially, but the GSTA tracks the desired attitude better when the signals approach the desired state. The RMSE values are slightly better for GSTA than PD and SMC along the second and third channel, while the PD is the best along the first. The SSE values are similar for all three controllers.

The angular velocity response shown in Figure 3 also highlights the performance difference between the PD controller and GSTA, where the curve of the latter follows a gentler slope. The angular velocity of the reaction wheels, as shown in Figure 4, are returned to their initial values after the reference changes at 30 seconds, except when using the PD controller. The magnetorquer response is similar for all three control laws, as seen in figure 6. The torque applied by the GSTA has a sharper slope than the

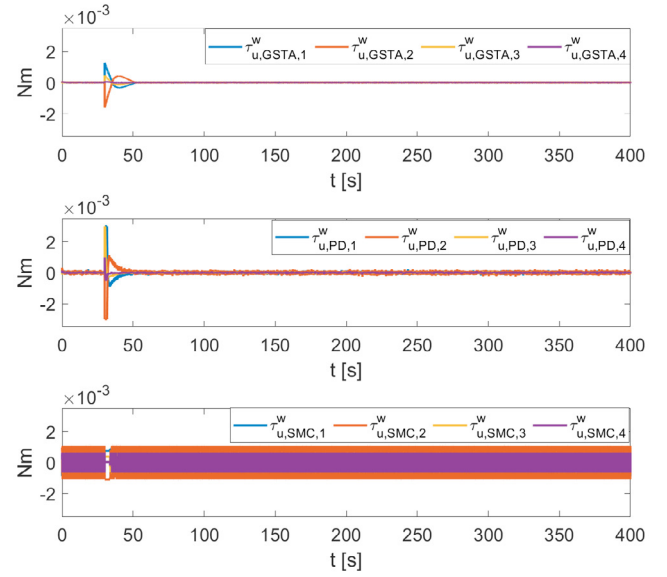


Fig. 5. Pointing: Plot of  $\tau_u^w$ .

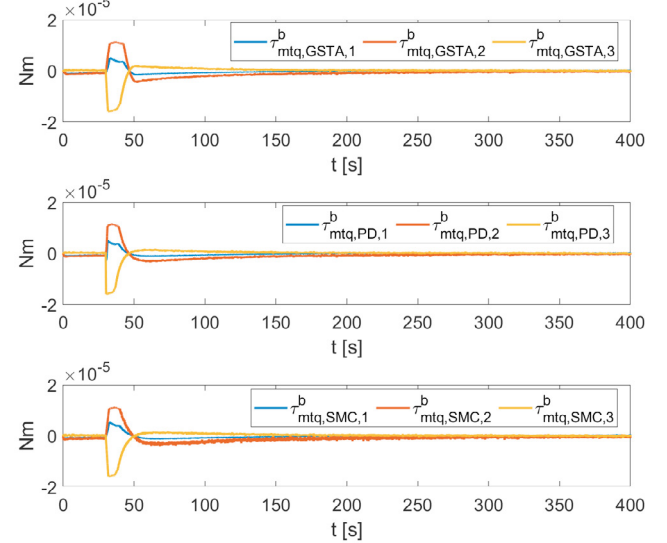


Fig. 6. Pointing: Plot of  $\tau_{mtq}^b$ .

SMC, as seen in Figure 5, causing a lot more torque to be applied to the reaction wheels after the system has settled. The PD controller has a higher peak and varies more than GSTA both before and after the transient period.

#### 4.4 Slewing

When the spacecraft is performing a slew maneuver, the angular velocity of the  $\{b\}$  relative to  $\{o\}$  is non-zero and constant. In this simulation, we choose a desired angular velocity about the  $y$ -axis. For slewing, the GSTA and the SMC use the surface defined in Equation (31).

The star (\*) in Table 7 denotes  $10^{-5}$  rad/s, and -1 indicates channels which start inside the error band and never leave, and therefore are always settled.

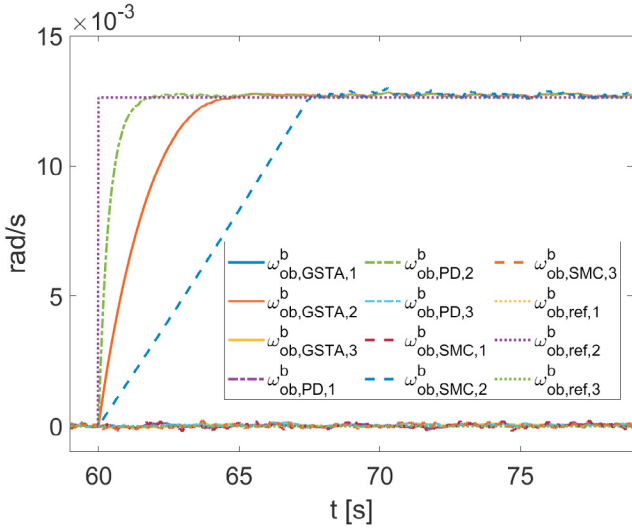
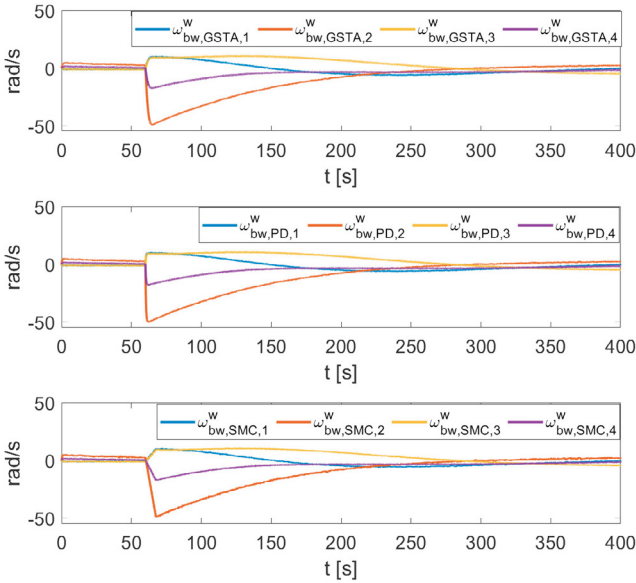
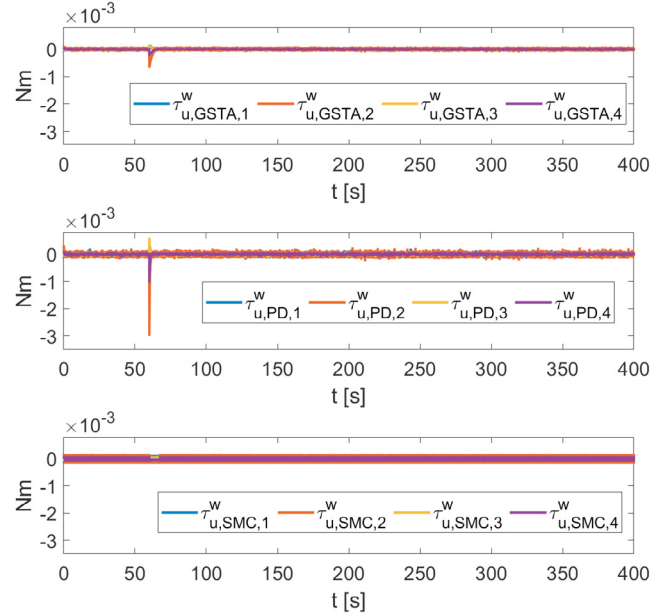
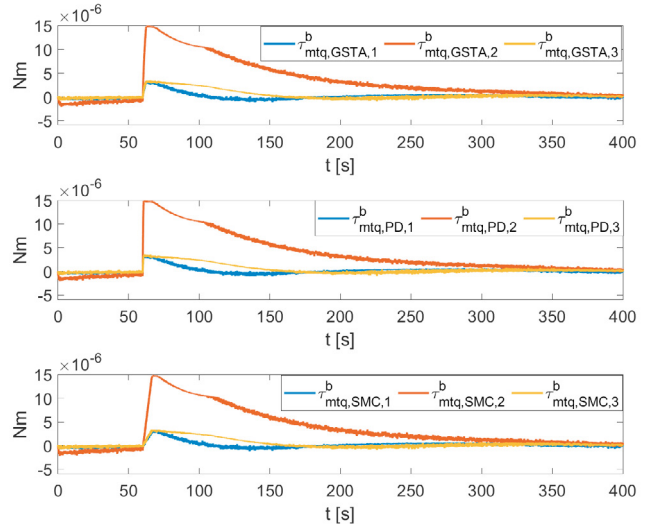

 Fig. 7. Slewing: Plot of  $\omega_{ob}^b$ .

 Fig. 8. Slewing: Plot of  $\omega_{bw}^w - \omega_{bw,ref}^w$ .

Table 7. Slewing performance

	Settling time	RMSE	SSE
GSTA	[-1, 3.63, -1]s	[3.91, 4.93, 4.95]*	[5.05, 0.30, 4.40]*
PD	[-1, 1.3, -1]s	[4.78, 5.32, 5.33]*	[3.73, 0.66, 5.08]*
SMC	[-1, 7.28, -1]s	[7.88, 11.1, 8.21]*	[5.99, 5.30, 11.7]*

The slow maneuver objective is shown in Figure 7. In general, the GSTA outperforms the SMC when considering settling time. However, the PD controller performs better as shown clearly in Figure 7 and Table 7. The GSTA uses 3.63 seconds, while the SMC uses 7.28 seconds to settle about the  $y$ -axis. For comparison, the PD controller uses just 1.3 seconds. Note that the inclination of the sliding surface used for slewing, the positive definite constant  $c_1$  from Equation (31), is different for the GSTA and the SMC algorithm, as specified in Table 5. This is due to the SMC algorithm overshooting the reference if the chosen value is


 Fig. 9. Slewing: Plot of  $\tau_u^w$ .

 Fig. 10. Slewing: Plot of  $\tau_{mtq}^b$ .

too high. By decreasing  $c_1$  from the value set for GSTA, the SMC manages to control the system. Furthermore, the GSTA performs well with both of the given  $c_1$  values.

It is possible to increase the SMC gain to lower the settling time, but this would increase the RMSE values, and the SMC might be unable to settle within the error band in a chosen time period. Even with the current values, the SMC has a significantly higher RMSE than GSTA and PD controller for slewing.

Increasing the gain for the GSTA to lower the settling time would increase the RMSE value as well, which are slightly better than those of the PD controller with the current parameters.

For reaction wheel speed, it can be seen in Figure 8 that the momentum dumping controller uses longer time to reach the initial speed values compared pointing, as seen in Figure 4. To improve this, the reference angular momentum must be updated in a slew maneuver as shown in (Grøtte et al., 2020). Figure 10 shows that the magnetorquers produce high frequency signals as in pointing, but of a different shape than those in Figure 6 as it counteracts a different change in wheel speed. The torque plot for the attitude control algorithms, Figure 9, show that the GSTA has a spike around the change in reference at 60 seconds, while the amplitude of the SMC signal has a fixed maximum value. Note that the peak value of the PD controller is significantly higher than the peak of the GSTA, and the signal is more contaminated by noise for the PD controller, as shown in Figure 5.

## 5. CONCLUSION

In this paper we have studied the performance of three different control algorithms applied to attitude control of a spacecraft actuated with reaction wheels: the GSTA, SMC, and PD controller. The simulation results show that the GSTA control chatter is greatly reduced when compared to SMC. Overall attitude control performance is improved when comparing GSTA to SMC in a slew maneuver. GSTA displays similar accuracy as the PD controller under the given conditions, but with lower spikes and less chatter in the torque applied to the reaction wheels. The settling time for the GSTA is shorter for pointing, but longer for slewing when compared to a well-tuned PD controller.

## REFERENCES

- Borlaug, I.L.G., Pettersen, K.Y., and Gravdahl, J.T. (2019). Tracking control of an articulated intervention AUV in 6DOF using the generalized super-twisting algorithm. In *2019 American Control Conference (ACC)*, 5705–5712.
- Castillo, I., Fridman, L., and Moreno, J.A. (2018). Super-Twisting Algorithm in presence of time and state dependent perturbations. *Int. J. Control*, 91(11), 2535–2548.
- Crassidis, J.L. and Markley, F.L. (1996). Sliding mode control using modified Rodrigues parameters. *J. Guid. Control Dyn.*, 19(6), 1381–1383.
- Egeland, O. and Gravdahl, J.T. (2002). *Modeling and simulation for automatic control*, volume 76. Marine Cybernetics Trondheim, Norway.
- Fjellstad, O.E. and Fossen, T. (1994). Singularity-free tracking of unmanned underwater vehicles in 6 DOF. In *Proc. of 1994 33rd IEEE Conference on Decision and Control*, volume 2, 1128–1133 vol.2.
- Gravdahl, J.T., Eide, E., Skavhaug, A., Fauske, K.M., Svartveit, K., and Indergaard, F.M. (2003). Three axis Attitude Determination and Control System for a Picosatellite: Design and Implementation. In *Proc. of the 54th Int. Astronautical Congress*. American Institute of Aeronautics and Astronautics, Bremen, Germany.
- Grøtte, M.E., Gravdahl, J.T., Johansen, T.A., Larsen, J.A., Vidal, E.M., and Surma, E. (2020). Spacecraft Attitude and Angular Rate Tracking using Reaction Wheels and Magnetorquers. In *Proc. of the 2020 IFAC World Congress*.
- Hughes, P.C. (2004). *Spacecraft Attitude Dynamics*. Dover Publications, Mineola, New York.
- Janardhanan, S., un Nabi, M., and Tiwari, P.M. (2012). Attitude control of magnetic actuated spacecraft using super-twisting algorithm with nonlinear sliding surface. In *2012 12th Int. Workshop on Variable Structure Systems*, 46–51.
- Kristiansen, R., Nicklasson, P., and Gravdahl, J. (2009). Satellite Attitude Control by Quaternion-Based Backstepping. *IEEE Trans. Control Syst. Technol.*, 17, 227 – 232.
- Krogstad, T.R. and Gravdahl, J.T. (2006). 6-DOF mutual synchronization of formation flying spacecraft. In *Proc. of the 45th IEEE Conference on Decision and Control*, 5706–5711.
- Levant, A. (1993). Sliding order and sliding accuracy in sliding mode control. *Int. J. Control*, 58(6), 1247–1263.
- Markley, F.L. and Crassidis, J.L. (2014). *Fundamentals of spacecraft attitude determination and control*, volume 33. Springer.
- McDuffie, J. and Shtessel, Y. (1997). A de-coupled sliding mode controller and observer for satellite attitude control. In *Proc. The Twenty-Ninth Southeastern Symposium on System Theory*, 92–97.
- Oland, E. and Schlanbusch, R. (2009). Reaction wheel design for CubeSats. In *2009 4th Int. Conference on Recent Advances in Space Technologies*, 778–783.
- Shrivastava, S.K. and Modi, V.J. (1983). Satellite attitude dynamics and control in the presence of environmental torques-A brief survey. *J. Guid. Control Dyn.*, 6(6), 461–471.
- Shtessel, Y., Edwards, C., Fridman, L., and Levant, A. (2014). *Sliding mode control and observation*. Springer.
- Wen, J.Y. and Kreutz-Delgado, K. (1991). The attitude control problem. *IEEE Trans. Automat. Contr.*, 36(10), 1148–1162.